

Numerical studies of dispersion due to tidal flow through Moskstraumen, northern Norway

Birgit Kjoss Lyngre · Jarle Berntsen · Bjørn Gjevik

Received: 24 March 2010 / Accepted: 20 May 2010 / Published online: 27 June 2010
© Springer-Verlag 2010

Abstract The effect of horizontal grid resolution on the horizontal relative dispersion of particle pairs has been investigated on a short time scale, i.e. one tidal M_2 cycle. Of particular interest is the tidal effect on dispersion and transports in coastal waters where small-scale flow features are important. A three-dimensional ocean model has been applied to simulate the tidal flow through the Moskstraumen Maelstrom outside Lofoten in northern Norway, well known for its strong current and whirlpools (Gjevik et al., *Nature* 388(6645):837–838, 1997; Moe et al., *Cont Shelf Res* 22(3):485–504, 2002). Simulations with spatial resolution down to 50 m have been carried out. Lagrangian tracers were passively advected with the flow, and Lyapunov exponents and power law exponents have been calculated to analyse the separation statistics. It is found that the relative dispersion of particles on a short time scale

(12–24 h) is very sensitive to the grid size and that the spatial variability is also very large, ranging from 0 to 100 km² over a distance of 100 m. This means that models for prediction of transport and dispersion of oil spills, fish eggs, sea lice etc. using a single diffusion coefficient will be of limited value, unless the models actually resolves the small-scale eddies of the tidal current.

Keywords Relative dispersion · Grid resolution · Tidal current · Whirlpool · Particle tracking · Lyapunov

1 Introduction

Accurate model prediction of relative dispersion of particle pairs in complex current fields can be of considerable value for several practical purposes, i.e. oil spill, dispersion of sea lice and pollutants. An important question is what horizontal grid resolution is required to predict dispersion accurately on different time scales, from short time scales, i.e. one tidal cycle to long time scales like months and years. The effect of Eulerian spatial resolution on drifting particle pairs has recently been studied extensively by Poje et al. (2010) with an examination of several ocean models, a two-dimensional turbulence model, ROMS and HYCOM, on grid scales from 0.5 to 8 km and on time scales from tidal periods to several months. Understanding the properties of dispersion is also important in studies of drifters and tracers, see, e.g. LaCasce (2008) and Haza et al. (2007).

In many areas in coastal waters, flow and dispersion is driven by the barotropic tide. Tidal effects on dispersion and transports are hence of particular interest and

Responsible Editor: John Grue

B. K. Lyngre (✉)
Norwegian Hydrographic Service, Stavanger, Norway
e-mail: birgit-kjoss.lyngre@statkart.no

J. Berntsen
Department of Mathematics, University of Bergen,
P.O. Box 7803, 5020 Bergen, Norway
e-mail: jarle.berntsen@math.uib.no

B. Gjevik
Department of Mathematics, University of Oslo,
P.O. Box 1053, Blindern, 0316, Oslo, Norway
e-mail: bjorn@math.uio.no

Present Address:

B. K. Lyngre
Department of Mathematics, University of Oslo,
P.O. Box 1053, Blindern, 0316, Oslo, Norway

have been studied by several authors, e.g. Zimmerman (1986), Geyer and Signell (1992), Signell and Butman (1992), Ridderinkhof and Zimmerman (1992), Gjevik (1996) and Orre et al. (2006) and references therein.

Our focus in this paper will be on the horizontal relative dispersion of particle pairs in tidal currents on a short time scale when small-scale flow features are important. The site for our investigation is the Moskstraumen Maelstrom outside Lofoten on the northern coast of Norway (see Fig. 1) where the current fields are known both from two-dimensional and three-dimensional modelling. Moskstraumen is well known for its strong current and whirlpools, see Gjevik et al. (1997) and Moe et al. (2002). Tidal-driven currents dominate wind-driven currents in the area. The significant difference in tidal amplitude in Vestfjorden and the shelf outside Lofoten combined with a complex bathymetry causes strong tidal currents running with total strength up to $3\text{--}5\text{ ms}^{-1}$.

New technology like increased computing power and high-resolution bottom topography available from multibeam surveys enable us to resolve small-scale flow feature with improved accuracy. The Bergen ocean model (Berntsen 2000) has been used for simulations with 50, 100, 200, 400 and 800 m grid resolution. The objective is to investigate the sensitivity of dispersion to the horizontal grid size Δx , Δy . Simulations with both homogeneous conditions and stratification have been carried out in order to study the sensitivity of dispersion to the density field $\rho(z)$.

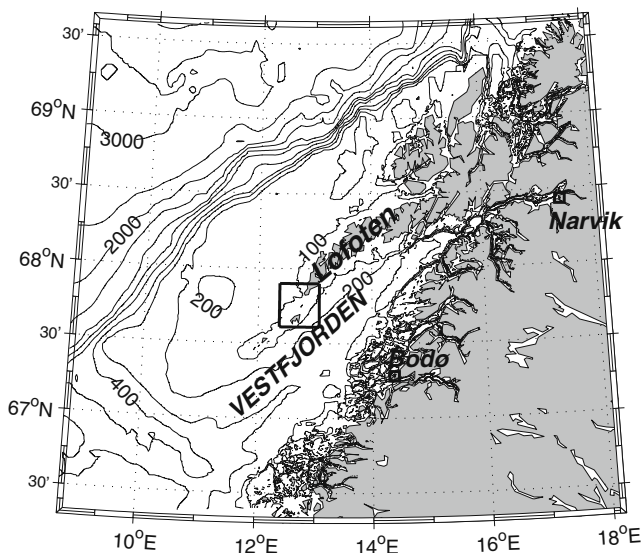


Fig. 1 Location of the model domain on the northern coast of Norway. Model domain is marked with a square box in the area of Lofoten. Contour lines show the bottom topography in the area with depth in metres

Processes affecting the transport and dispersion of fish eggs and larvae on long time scales (i.e. month-years) has been studied previously. The periodical tidal current in Moskstraumen combined with background currents of order $0.1\text{--}0.3\text{ ms}^{-1}$ from the Norwegian Coastal Current is found to introduce a tidal pumping between Vestfjorden inside Lofotodden and the shelf outside (Ommundsen 2002). Aadlandsvik (1994) and Vikebø et al. (2007) simulated the transport of eggs/larvae/juveniles of Arcto-Norwegian cod from the Lofoten area with a coarse grid model that only resolve the large-scale flow features which are important for dispersion on long time scales. The area of Vestfjorden and the Lofoten Islands is a region with complex circulation dominated by the two major currents, the Norwegian Coastal Current and the Norwegian Atlantic Current. Mitchelson-Jacob and Sundby (2001) discuss how complex bathymetry in the area and interaction with tidal currents can modify these major currents and induce mesoscale eddies, with diameter 20–60 km, revealed in the Vestfjord basin by satellite tracked drifters. Slagstad and Tande (2007) and Skarðhamar et al. (2007) investigated transport and distribution of plankton on the shelf area of Northern Norway.

Strong tidal currents have a crucial effect on dispersion and drift of pollutants in coastal waters. Transport of pollutants, for instance from oil spills and industrial activity, transport of sea lice or diseases from fish farms and transport of discharged sewage may affect the water quality and the natural marine ecosystems. Dispersion of oil spill was studied by Proctor et al. (1994). After M.V. *Braer* ran aground near the southern tip of the Shetland Island in January 1993, they used a high-resolution model in an area with strong tidal current for forecast and hindcast simulations of the oil spill. Davies et al. (2000) investigated the spatial distribution of currents and waves at the time of the *Braer* accident with a high-resolution model. They found that it is essential to take account of wind wave turbulence when modelling transport of pollutants in the surface layer during major wind events. The oil spill model OSCAR is described in Reed et al. (1999a, b) which also provide a review of oil spill modelling. There is also several works on dispersion of sea lice and diseases from fish farms, e.g. Amundrud and Murray (2009) and Gillibrand and Willis (2007).

2 The numerical model

The σ -coordinate ocean model (Bergen ocean model) applied in the present studies is a three-dimensional

(x, y, z) model described in Berntsen (2000) where x and y are the horizontal Cartesian coordinates and z the vertical coordinate. The model applies the Boussinesq approximation and is here applied in a hydrostatic form. It is available from www.math.uib.no/BOM/. The model has recently been used for idealized studies of internal wave generation and mixing of flow over sills (Berntsen et al. 2008, 2009). The governing equations are:

The continuity equation,

$$\nabla \times \mathbf{u} + \frac{\partial w}{\partial z} = 0, \tag{1}$$

and the Reynolds momentum equations,

$$\frac{\partial u}{\partial t} + \mathbf{u} \times \nabla u + w \frac{\partial u}{\partial z} - fv = -\frac{1}{\rho_0} \frac{\partial p}{\partial x} + \frac{\partial}{\partial z} \left(A_v \frac{\partial u}{\partial z} \right) + F_x, \tag{2}$$

$$\frac{\partial v}{\partial t} + \mathbf{u} \times \nabla v + w \frac{\partial v}{\partial z} + fu = -\frac{1}{\rho_0} \frac{\partial p}{\partial y} + \frac{\partial}{\partial z} \left(A_v \frac{\partial v}{\partial z} \right) + F_y, \tag{3}$$

$$\rho g = -\frac{\partial p}{\partial z}. \tag{4}$$

In the equations above, $\mathbf{u} = (u, v)$ is the horizontal velocity field, w the vertical velocity, t the time, f Coriolis parameter, g is gravity, ρ is the density, ρ_0 is the reference density, p is pressure and A_v vertical eddy viscosity. The conservation equations for temperature T and salinity S are given by

$$\begin{aligned} \frac{\partial(T, S)}{\partial t} + \mathbf{u} \times \nabla(T, S) + w \frac{\partial(T, S)}{\partial z} \\ = \frac{\partial}{\partial z} \left(K_v \frac{\partial(T, S)}{\partial z} \right) + F_{T,S}, \end{aligned} \tag{5}$$

where K_v is the vertical eddy diffusivity. The horizontal eddy viscosity terms F_x and F_y and the horizontal diffusivity terms F_T and F_S are given by

$$F_{x,y} = \frac{\partial}{\partial x} \left(A_h \frac{\partial(u, v)}{\partial x} \right) + \frac{\partial}{\partial y} \left(A_h \frac{\partial(u, v)}{\partial y} \right), \tag{6}$$

$$F_{S,T} = \frac{\partial}{\partial x} \left(K_h \frac{\partial(S, T)}{\partial x} \right) + \frac{\partial}{\partial y} \left(K_h \frac{\partial(S, T)}{\partial y} \right), \tag{7}$$

where A_h is the horizontal eddy viscosity and K_h the horizontal diffusivity.

The total pressure P is given by the pressure due to the free surface elevation η and the internal pressure, $P = g\rho_0\eta + g \int_z^0 \rho(\hat{z})d\hat{z}$. The internal pressure is neglected for the homogeneous case.

The variables are discretized on a C-grid. In the vertical, the standard σ -transformation, $\sigma = \frac{z-\eta}{H+\eta}$, where

H is the bottom depth, is applied. For advection of momentum and density a total variance diminishing (TVD) scheme with a superbee limiter described in Yang and Przekwas (1992) is applied in the present studies. The standard second-order Princeton ocean model method is applied to estimate the internal pressure gradients (Blumberg and Mellor 1987; Mellor 1996). The model is mode split with a method similar to the splitting described in Berntsen et al. (1981) and Kowalik and Murty (1993).

The time steps are performed with a predictor–corrector method both in the internal time steps and in the external time steps. The leapfrog method is used as the predictor, and the fully implicit method is used as the corrector.

2.1 Model setup and boundary conditions

High-resolution bottom topography based on multi-beam bathymetric data from the Norwegian Hydrographic Service is used to generate the bottom matrices. The topography is shown in Fig. 2. Horizontally, the grids applied are equidistant and the experiments are run with horizontal grid size $\Delta x = \Delta y$ equal to 50, 100, 200, 400 and 800 m in order to investigate how the dispersion is affected by the grid size. In the vertical, ten equidistant σ -layers are used in all experiments

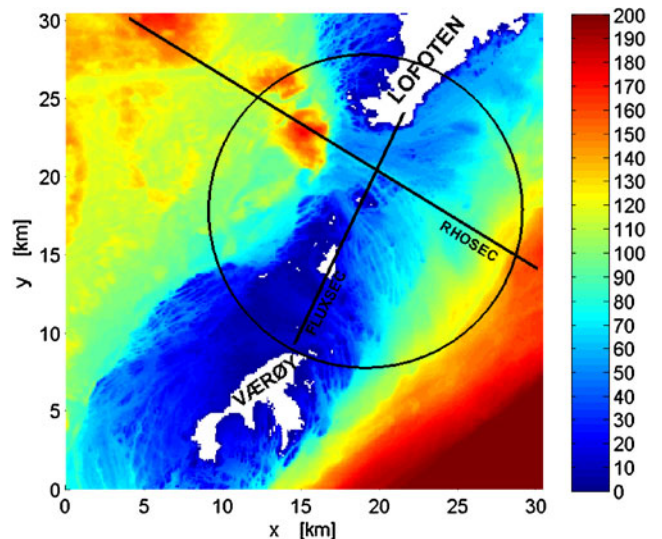


Fig. 2 Bottom topography for the model area with the island Værøy in southwest, Lofotodden in the north and the island Mosken in between. Colour bar is depth in metres. The figure also shows a circle with radius 10 km for calculations of mean relative dispersion R^2 , a section (RHOSec) for density field $\rho(z)$ and a section (FLUXSEC) for volume flux through Moskstraumen

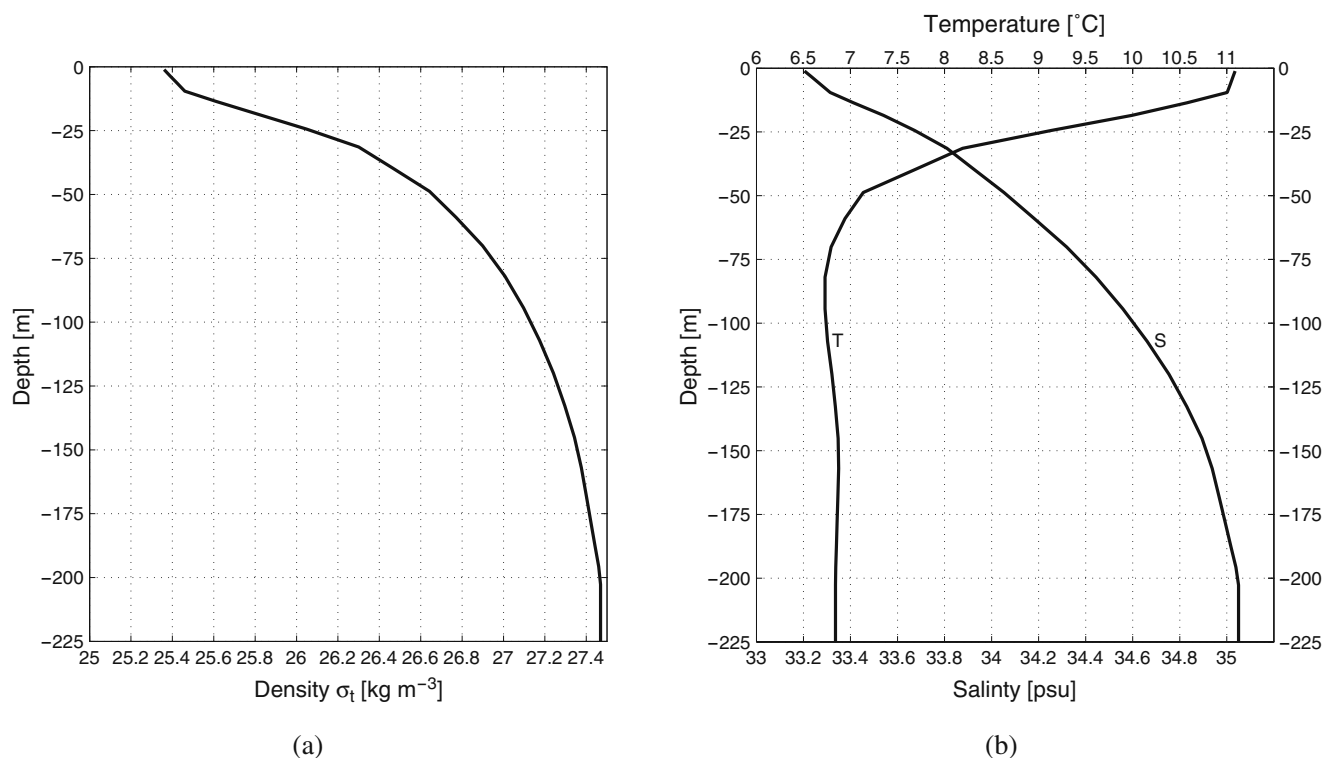


Fig. 3 Profiles for the stratification used in the experiments. **a** Density and **b** salinity and temperature

(seven layers for the 50-m grid due to limited memory on the available computer). In the experiments with $\Delta x = 50$ m the internal time step used is 3 s, and 30 external time steps are used for each internal step. The time steps are scaled proportionally with Δx in the experiments with other grid resolutions in order to keep the Courant number equal in all experiments. The simulations are carried out for both homogenous conditions and with stratification. For the stratified case, horizontally uniform fields of temperature and salinity representative for the area (from Engedahl et al. 1998) are used as initial conditions. The vertical profiles of temperature, salinity and density, typical for a summer situation with strong stratification, are given in Fig. 3. The Coriolis frequency f is equal to $1.3 \times 10^{-4} \text{ s}^{-1}$.

There is no flow through the sea bed or the closed lateral boundaries. Free slip boundary conditions are

applied at the lateral boundaries in computing the non-linear momentum advection term. Initially, the water elevation is zero and there is no flow.

As a driving force, tidal elevation represented by the main diurnal constituent M_2 is forced into the model domain through the open boundaries. Experiments with additional tidal components are studied by Orre et al. (2006) in Trondheimsleia. They conclude that adding the next most energetic tidal constituent S_2 has only minor effects on the dispersion. We therefore focus on dispersion due to M_2 tide in this work. Amplitude and phase are specified in every grid cell at the boundary, and the tidal elevation is calculated and given for every time step.

At the open boundaries, ten grid cells wide flow relaxation zones (Martinsen and Engedahl 1987) are added to the computational domain. In the flow

Table 1 Mean value of $R^2(T) \times 10^{-6}$ in a circle in Moskstraumen of radius 10 km, as a function of Δx and δ for the stratified case

Δx (m)	$R^2(T) \times 10^{-6}$ (m ²)		δ (m)							
	50	100	50	100	200	400	800	1,600	2,400	3,200
50	12.787	18.915	27.517	38.964	56.257	81.186	104.540	125.955		
100		15.580	24.525	37.187	54.683	79.980	98.009	111.842		
200			14.755	27.010	44.983	71.437	92.568	107.611		
400				11.589	23.118	45.051	65.133	84.470		
800					5.689	15.036	26.928	38.455		

T is time at the end of the M_2 period

Table 2 Sensitivity of the Lyapunov exponent λ and the power law exponent c_1 for $\delta = 800$ m to the grid size Δx for the stratified (strat) and the homogeneous (hom) experiments

Δx (m)	$\lambda(\text{strat})$ (day ⁻¹)	$\lambda(\text{hom})$ (day ⁻¹)	$c_1(\text{strat})$	$c_1(\text{hom})$
50	4.260	3.932	1.611	1.591
100	4.171	4.135	1.606	1.604
200	4.151	4.114	1.579	1.571
400	3.518	3.895	1.538	1.541
800	2.079	2.610	1.415	1.441

relaxation zone, the water elevation is updated in each time step according to

$$\phi = (1 - \alpha)\phi_{\text{int}} + \alpha\phi_{\text{ext}}, \tag{8}$$

where ϕ_{int} contains the unrelaxed values computed by the model and ϕ_{ext} is a specified external value. The relaxation parameter α varies smoothly from 1 at the open boundary to 0 at the innermost cell of the boundary zone, see Martinsen and Engedahl (1987).

The experiments are performed with constant values of vertical eddy viscosity $A_v = 2 \times 10^{-3} \text{ m}^2 \text{ s}^{-1}$ and vertical eddy diffusivity $K_v = 10^{-7} \text{ m}^2 \text{ s}^{-1}$. The horizontal eddy viscosity A_h is computed according to Smagorinsky (1963), by

$$A_h = C_h \Delta x \Delta y \frac{1}{2} \left[\left(\frac{\partial u}{\partial x} \right)^2 + \frac{1}{2} \left(\frac{\partial v}{\partial x} + \frac{\partial u}{\partial y} \right)^2 + \left(\frac{\partial v}{\partial y} \right)^2 \right]^{\frac{1}{2}}, \tag{9}$$

where C_h is a constant. In the mode split model, the horizontal velocity components u and v are split according to $u = \bar{u} + u'$ and $v = \bar{v} + v'$ where \bar{u} and \bar{v} are the depth averaged values and u' and v' the corresponding deviations. The viscosity A_h is acting on u' and v' . The same expression as in Eq. 9, with \bar{u} and \bar{v} replacing u and v and C_{h2d} replacing C_h , is used to compute the horizontal eddy viscosity A_{h2d} acting on the \bar{u} and \bar{v} . In our experiments, $C_h = 0.25$ and $C_{h2d} = 2.0$ except in the experiments with $\Delta x = 50$ m where $C_h = 0.5$

Table 3 Sensitivity of the Lyapunov exponent λ and the power law exponent c_1 for $\Delta x = 100$ m to the initial separation δ

δ (m)	$\lambda(\text{strat})$ (day ⁻¹)	$\lambda(\text{hom})$ (day ⁻¹)	$c_1(\text{strat})$	$c_1(\text{hom})$
100	6.893	6.704	1.392	1.382
200	6.040	5.829	1.465	1.455
400	5.120	4.996	1.537	1.531
800	4.171	4.135	1.606	1.604
1600	3.240	3.236	1.675	1.671
2400	2.672	2.695	1.703	1.707
3200	2.239	2.306	1.721	1.726

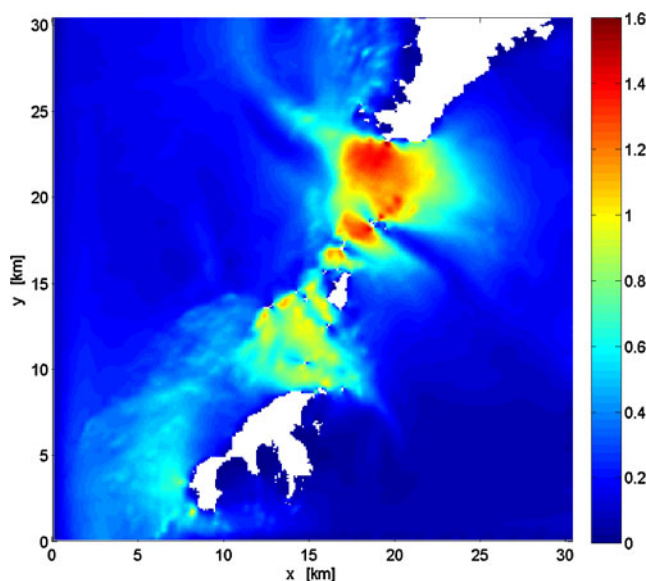


Fig. 4 Semi-major current axis for the M_2 tidal current. Colour bar is current speed in metres per second

and $C_{h2d} = 4.0$ for the stratified case, and $C_h = 1.0$ and $C_{h2d} = 8.0$ for the homogeneous case to ensure stability. The coefficients C_{h2d} acting on the depth averaged flow need to be larger than C_h due to the strong tidal inflow which primarily forces the depth averaged velocity components. The horizontal diffusivity K_h is chosen to be zero, see the discussion below.

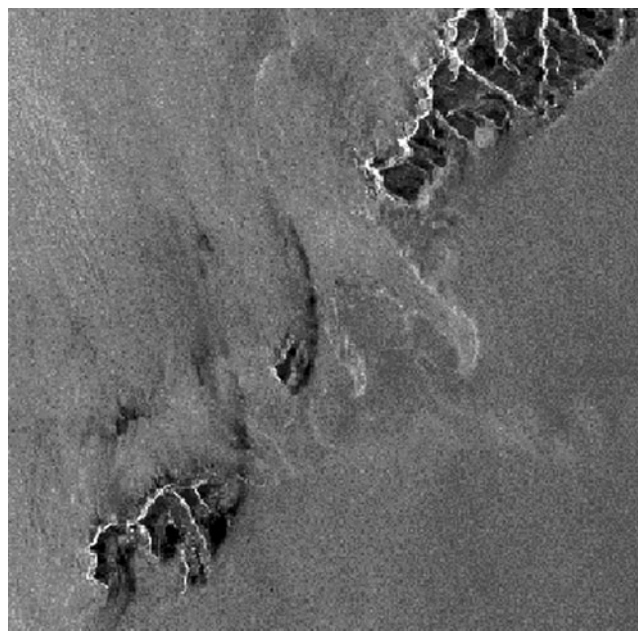


Fig. 5 SAR image (ERS1-SAT) from Moskstraumen 20. August 1994. The headland of Lofoten in the upper right corner. The scene is from about 2 h before ebb. From Wahl (1995)

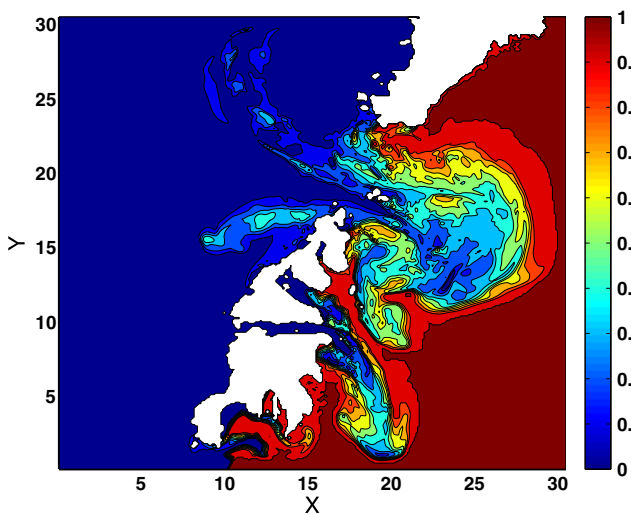


Fig. 6 Concentration at 10 m depth at the end of the M_2 period. Colour bar is concentration. Land contour to 10 m depth

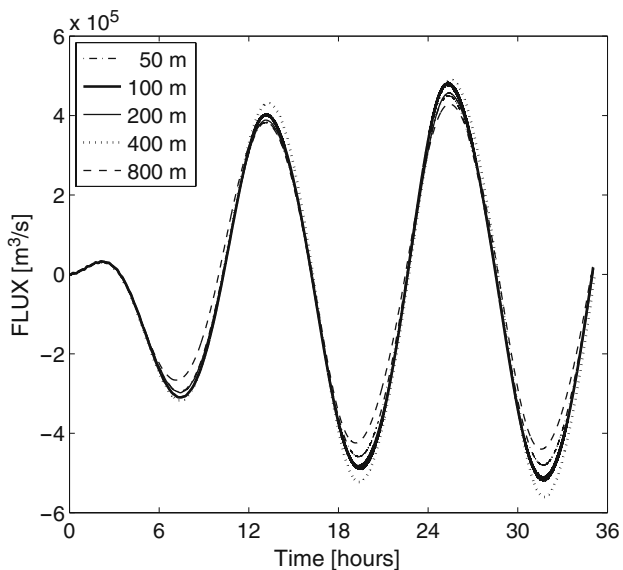
In studies like the present, unique optimal values of the viscosities and diffusivities may not be obtained. However, there are some general guidelines that we have tried to follow. For instance, the values must be large enough to filter out the grid scale noise and at the same time small enough to allow a best possible representation of the physical processes with the chosen grid size. The horizontal viscosity may be related to the horizontal shear, and this is often achieved by using

some version of the Smagorinsky scheme given above, see also Haidvogel and Beckmann (1999). To allow the representation of internal motion, the diffusivities are kept at a minimum level or zero. The mixing then becomes primarily controlled by the mixing associated with the TVD scheme. The vertical viscosity is often computed with the Mellor and Yamada (1982) scheme or some other Richardson number-dependent scheme. With the grid sizes used here, the vertical velocity shear may become strong. The Richardson numbers may accordingly become smaller than the critical value, and the mixing may become excessive even if the grid size is too coarse to represent overturning. A small and constant value of A_v is accordingly chosen in our experiments. It may also be noted that, in experiments like the present, the numerical viscosity and diffusivity may be substantial and of the same order of magnitude as the specified values, see Burchard and Rennau (2008) and Rennau and Burchard (2009). For further discussions, see Xing and Davies (2006a) and Berntsen et al. (2008, 2009).

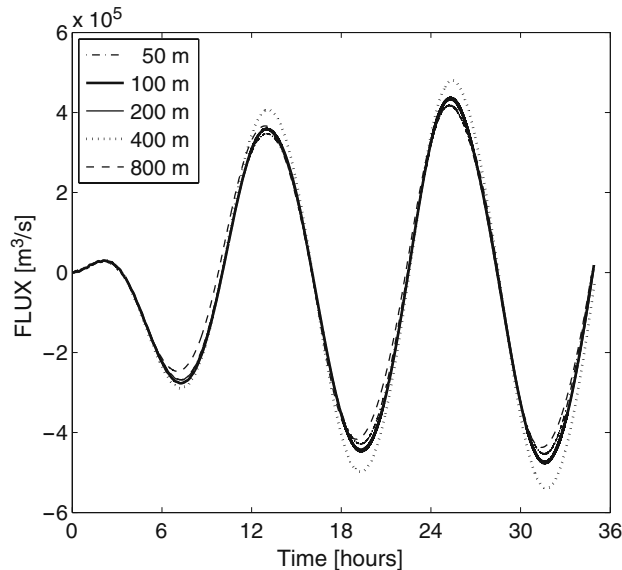
In the experiments, the bottom stress vector $\tau_b(x, t)$ is specified by

$$\tau_b(x, t) = \rho_0 C_D \sqrt{u_b^2 + v_b^2} \mathbf{u}_b(x, t), \tag{10}$$

where $\mathbf{u}_b = (u_b, v_b)$ and u_b and v_b are the velocity components in the lowermost grid cells in the x and y



(a)



(b)

Fig. 7 Volume flux through the section FLUXSEC in Moskstraumen. **a** Homogeneous conditions and **b** stratified conditions. West is positive direction

direction, respectively. The drag coefficient C_D is given by

$$C_D = \max \left[0.0025, \frac{\kappa^2}{(\ln(z_b/z_0))^2} \right], \tag{11}$$

where z_b is the distance of the nearest grid point to the bottom. The von Karman constant κ is 0.4 and the bottom roughness parameter is chosen to be $z_0 = 0.01$ m, see Blumberg and Mellor (1987).

The errors in the internal pressure gradients may be significant in σ -coordinate models, see for instance Haney (1991) and Mellor et al. (1998). In the present experiments with relatively small grid sizes, these errors are small. For instance in experiments with $\Delta x = 100$ m where the flow is driven only by the artificial internal pressure gradients, the absolute value of the volume flux through Moskstraumen remains smaller than $1 \times 10^3 \text{ m}^3 \text{ s}^{-1}$, which is about 0.2% of the flux for the stratified case for $\Delta x = 100$ m, see also Berntsen et al. (2008).

2.2 Particle tracking

In all experiments, Lagrangian tracers are released after an initial spin up of approximately two M_2 periods at the time when the flow turns westward out of Moskstraumen. The particles are released at an initial depth of 5 m and one particle in the middle of each horizontal cell. The Lagrangian tracers are advected passively with the flow over one M_2 period, and their positions are updated using the equation

$$\frac{d\mathbf{x}_k}{dt} = \mathbf{u}_{3d}(\mathbf{x}_k, t), \quad k = 1, \dots, M, \tag{12}$$

where $\mathbf{x}_k = (x_k, y_k, z_k)$ is the particle position and $\mathbf{u}_{3d} = (u, v, w)$ is the three-dimensional velocity field at the position of the particle. The subscript k indicates the particle number and M is the total number of particles released.

The relative horizontal dispersion is defined by

$$r_{i,j}(t) = (x_i(t) - x_j(t))^2 + (y_i(t) - y_j(t))^2, \tag{13}$$

where $(x_i(t), y_i(t))$ and $(x_j(t), y_j(t))$ are the horizontal coordinates at time t of particle pairs with subscripts i and j , initially released at a distance δ . It may be noted that vertical dispersion also affect the horizontal dispersion. Particles at different depths are quickly separated horizontally when the vertical shear is strong.

In order to investigate the mean horizontal relative dispersion in the Moskstraumen,

$$R^2(t) = \frac{1}{P} \sum_{i \neq j} r_{i,j}^2(t), \tag{14}$$

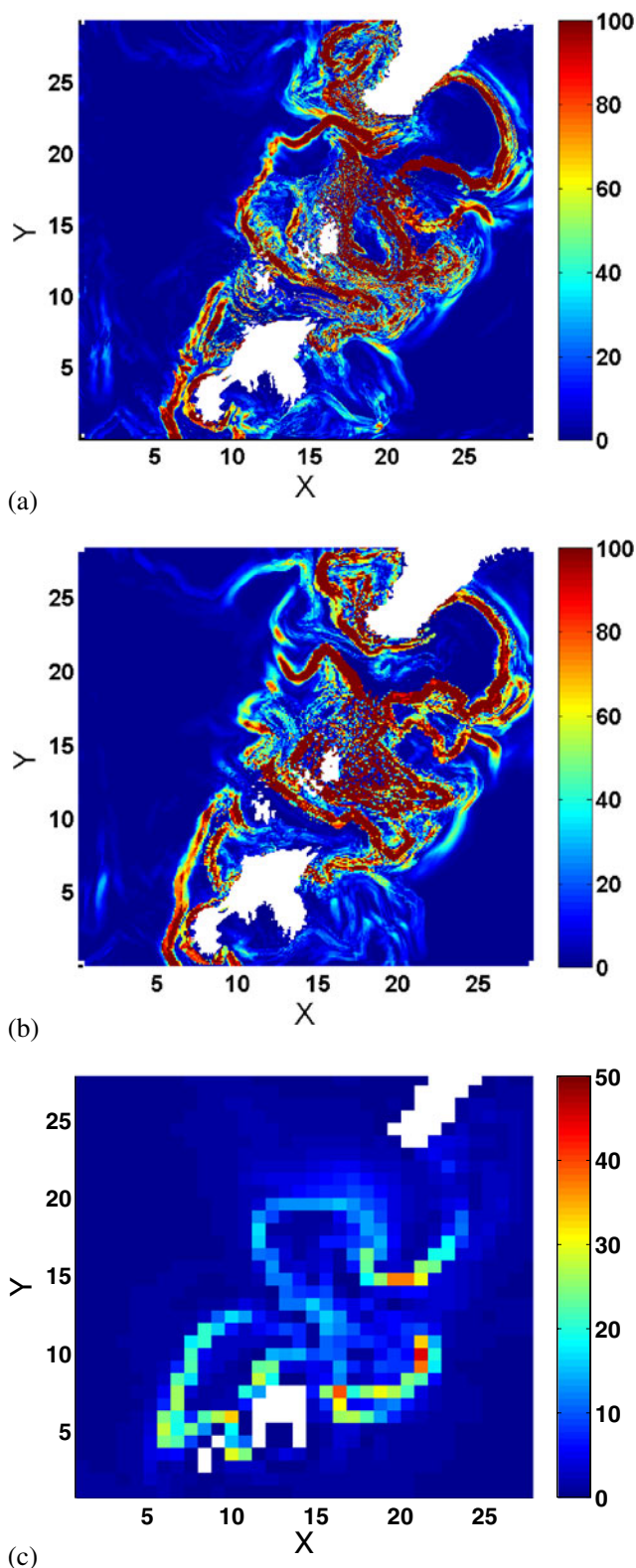


Fig. 8 Mean relative dispersion for each grid cell after one M_2 cycle calculated for the four particle pairs related to the particle in center of the grid cell. Initial distance of the particles is $\delta = 800$ m in x - y -direction. Results are given for **a** $\Delta x = 50$ m, **b** $\Delta x = 100$ m and **c** $\Delta x = 800$ m. Colour bar in square kilometres and distance on axis in kilometres

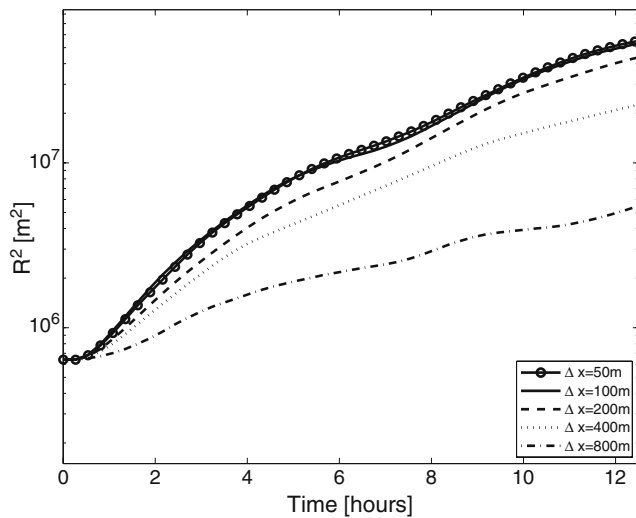


Fig. 9 Mean relative dispersion $R^2(t)$ for the stratified case for $\delta = 800$ m and $\Delta x = 50, 100, 200, 400$ and 800 m

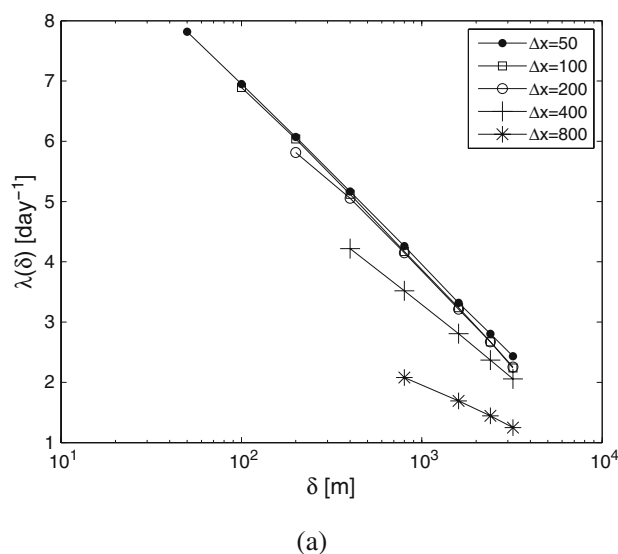
is computed over the M_2 period from the time of release, like in Orre et al. (2006). In Eq. 14, P is the number of particle pairs initially released inside a circle with radius 10 km, see Fig. 2.

For analysing of the separation statistics, the Lyapunov exponential model

$$R_L^2(t) \sim R^2(0)e^{2\lambda t} \tag{15}$$

and the power law model

$$R_P^2(t) \sim R^2(0) + t^{c_1}, \quad t > 0 \tag{16}$$



(a)

are used, see Orre et al. (2006) and Poje et al. (2010). For each experiment, best approximations in the least squares sense of $\ln R_L^2(t)$ and $\ln R_P^2(t)$ to $\ln R^2(t)$ are used to estimate the Lyapunov exponents λ in Eq. 15 and the power exponents c_1 in Eq. 16. For each grid size, the sensitivity of λ and c_1 to the initial distance δ is investigated. The sensitivity of these parameters to stratification is also explored, see Tables 1, 2 and 3.

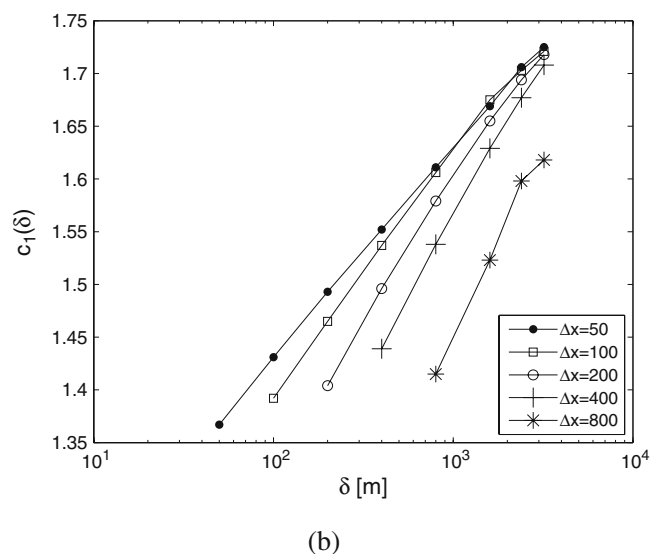
Following Poje et al. (2010), we define a mean relative diffusivity

$$K(t) = \frac{1}{2} \frac{dR^2}{dt} \tag{17}$$

where R^2 is the mean relative dispersion (Eq. 14).

3 Results

The σ -coordinate model, BOM, has been run for about three tidal periods of the main tidal constituent M_2 . The area of Moskstraumen exhibits strong tidal current with sharp horizontal shears. Figure 4 shows the semi-major axis of the main tidal constituent M_2 with a mean current of 1.5 ms^{-1} on the shallow ridge between the headland of Lofoten and Værøy consistent with the values in Gjevik et al. (1997) and Moe et al. (2002). The features of the tidal current in Moskstraumen can also be seen in the SAR image in Fig. 5. The sharp boundary between the east-going ebb tide current and the westward flood tide current closest to the headland of Lofoten is clearly visible in the image. In order to visualise the frontal structures in the model results, the



(b)

Fig. 10 **a** The Lyapunov exponent $\lambda(\delta)$ and **b** the power law exponent $c_1(\delta)$ as functions of δ and Δx inside the circle in Moskstraumen for the experiments with stratification

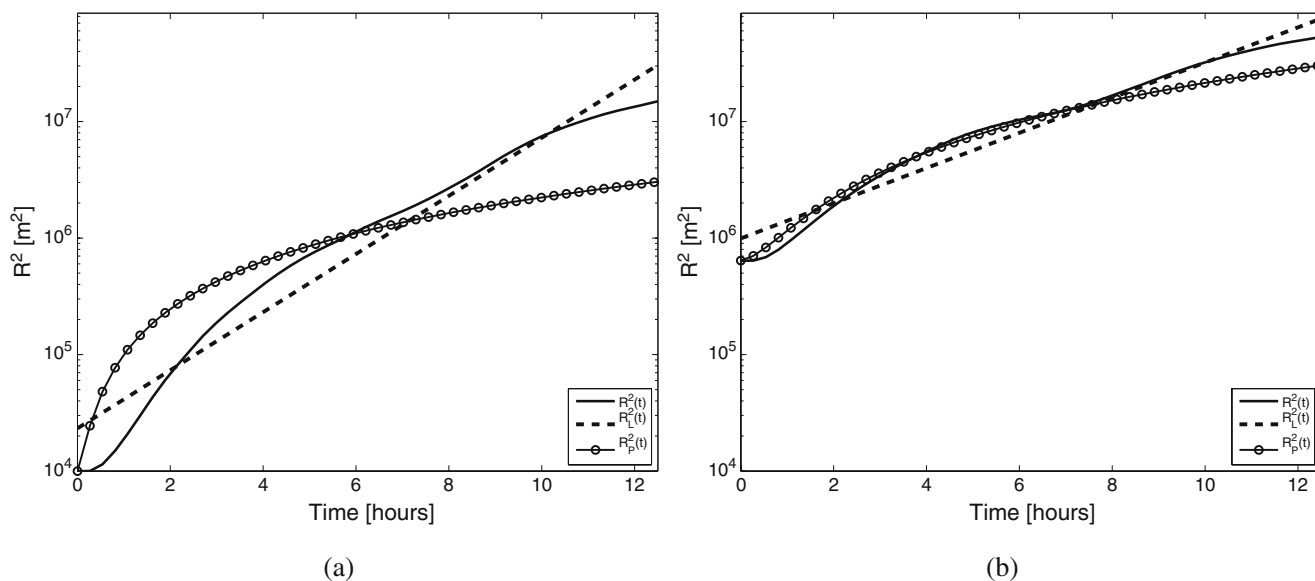


Fig. 11 Mean relative dispersion $R^2(t)$ together with the best approximations $R_L^2(t)$ and $R_P^2(t)$ for $\Delta x = 100$ m for the experiments with stratification. **a** Results for $\delta = 100$ m and **b** results for $\delta = 800$ m

water outside Moskstraumen was given concentration 0 and the water inside was given concentration 1 at the beginning of the last M_2 period in the simulation with 100 m grid size and with stratification. This concentration is propagated forward in time over one M_2 period using the same conservation Eq. 5 as for S and T . The same values of diffusivities as for S and T are also applied, i.e. the horizontal diffusivities are zero. The concentration at 10 m depth at the end of the M_2 period is given in Fig. 6 and shows that the fronts between

inside water and outside water are comparable to the features shown in the SAR image in Fig. 5.

Figure 7 gives the volume fluxes through a section of Moskstraumen (FLUXSEC in Fig. 2). The amplitudes of the fluxes in the last tidal cycle are approximately 0.4–0.5 Sv which is in accordance with Gjevik et al. (1997). These amplitudes are robust to the choice of grid size. The numerical experiments with 100 m grid resolution have been extended in time, and the amplitudes of the fluxes in subsequent tidal periods are

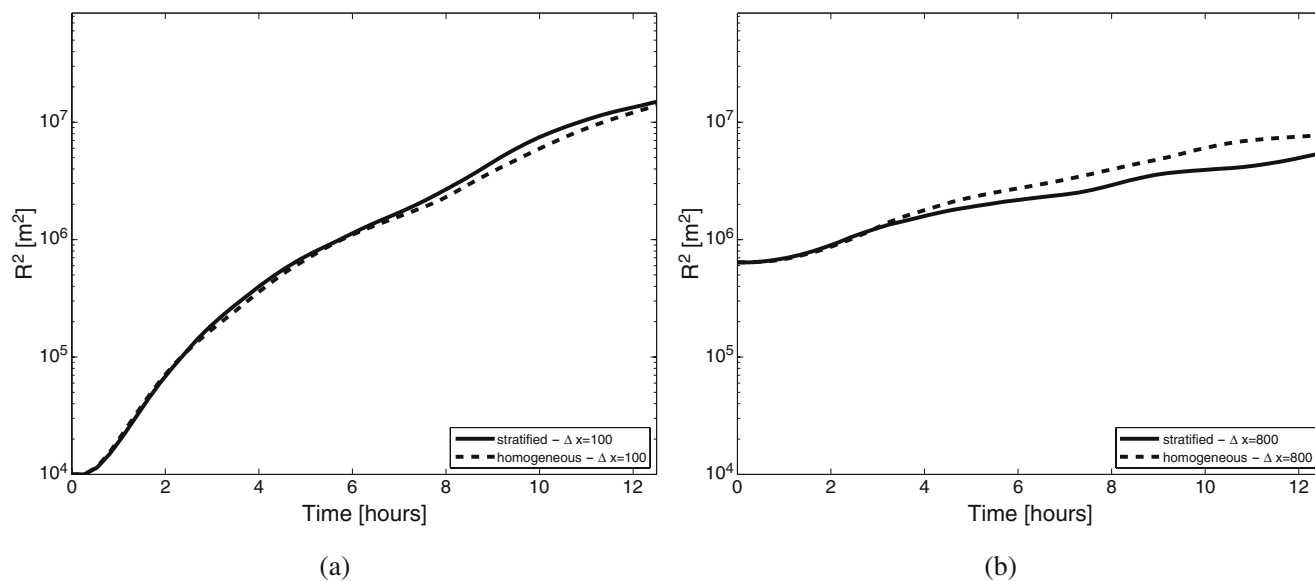


Fig. 12 Mean relative dispersion $R^2(t)$ for the stratified and homogeneous conditions. **a** $\Delta x = 100$ m and $\delta = 100$ m and **b** $\Delta x = 800$ m and $\delta = 800$ m

very similar to the amplitudes in the last tidal period given in Fig. 7. By comparing Fig. 7a, b, we find that stratification has only minor effects on these volume fluxes. The apparent robustness of the volume fluxes to stratification may partly be due to the choice of a constant value for the vertical diffusivity. With a Richardson number-dependent parameterization, the vertical profile of the current ellipse and the volume fluxes may be affected.

We will in the following focus on relative dispersion in the studies with stratification. The largest separation of particles occur in areas with sharp horizontal shear. The horizontal shear is best represented in the experiments with the highest spatial resolution. This may explain that the maximum values of relative dispersion are much higher in the results from the experiments with $\Delta x = 50$ m and $\Delta x = 100$ m than in the results from the experiment with $\Delta x = 800$ m, see Fig. 8. With higher spatial resolution, the smaller-scale features of the flow field are also in general better represented, and this is reflected in the large spatial variability of mean relative dispersion for each grid cell after one tidal cycle, see Fig. 8a, b.

The values of the mean relative dispersion $R^2(T)$, Eq. 14, where T is the time at the end of the M_2 period, also depend on the grid size, see Table 1. By comparing the values of $R^2(T)$ for a given initial distance δ , we find that the mean relative dispersion increases as the grid size is reduced. For a given value of δ , the relative changes of $R^2(T)$ are reduced when halving the grid size. This is for instance clearly seen by following the column for $\delta = 800$ m in Table 1 from the bottom to the top. The time series of $R^2(t)$ for this value of δ is given in Fig. 9. From Table 1 and Fig. 9, we find that the values of R^2 for $\Delta x = 50$ m and 100 m are fairly consistent. For small values of δ , the smaller-scale components of the flow field may contribute more to the initial increase of R^2 . The relative differences between the R^2 values for $\Delta x = 50$ and 100 m therefore tend to increase as δ is reduced, see also the discussion in Poje et al. (2010).

In order to analyse the growth of mean relative dispersion, the Lyapunov exponent λ , Eq. 15, and the power law exponent c_1 , Eq. 16, have been calculated for each experiment. The values of λ and c_1 for fixed initial distance $\delta=800$ m are given in Table 2. Both the Lyapunov exponents λ and c_1 are reduced for larger Δx , i.e. the growth of the mean relative dispersion $R^2(t)$ inside the circle in Moskstraumen is reduced with coarser grid resolutions. The values of λ and c_1 for fixed $\Delta x=100$ m as functions of δ are given in Table 3. The Lyapunov exponent λ increases as $\delta \rightarrow 0$. This is also shown in Fig. 10a where λ and c_1 are given as functions of δ . The rate of growth of mean relative dispersion

increases with finer grid resolutions and smaller values of δ . While λ increases as $\delta \rightarrow 0$, the power law exponent c_1 decreases as $\delta \rightarrow 0$, see Table 3 and Fig. 10b. Figure 10 also shows a convergence of the Lyapunov exponent λ and the power law exponent c_1 for the different grid resolutions Δx as the values of δ increase, while the values of λ and c_1 are more sensitive to the grid size for the smallest values of δ .

Figure 11 shows $R^2(t)$ for the simulation with $\Delta x = 100$ m for $\delta = 100$ m and $\delta = 800$ m together with the best approximations $R_L^2(t)$, Eq. 15, and $R_P^2(t)$, Eq. 16.

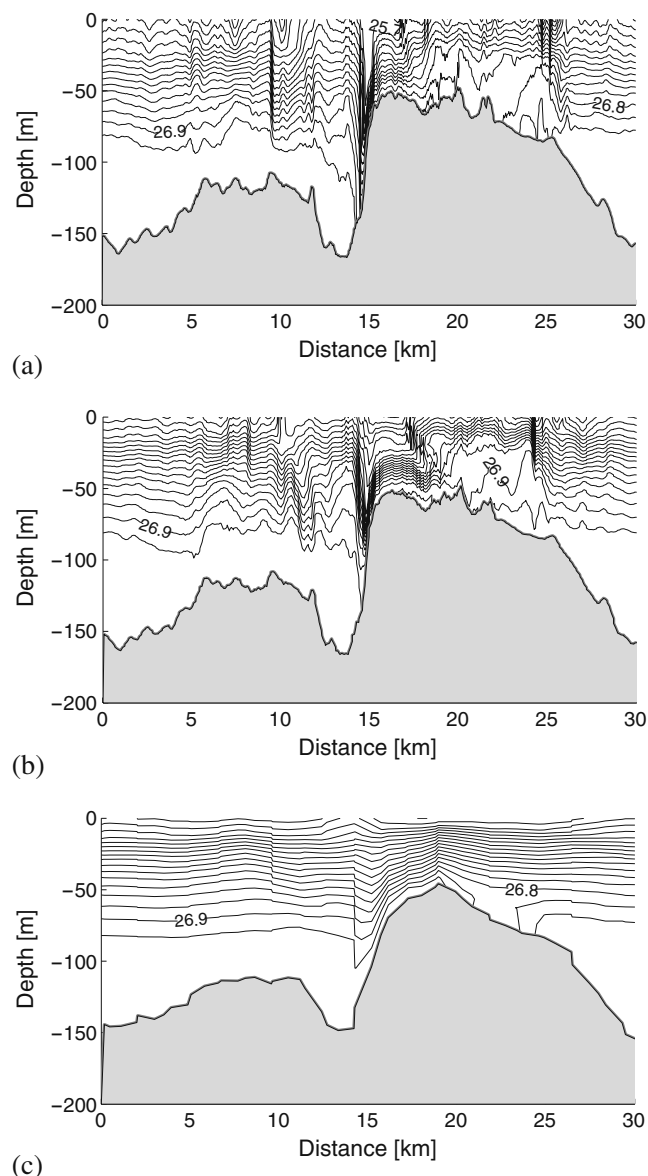


Fig. 13 Density field σ_t (kilograms per cubic metre) from the section RHOSEC in Fig. 2 at maximum outflow for **a** $\Delta x = 50$ m, **b** $\Delta x = 100$ m and **c** $\Delta x = 800$ m. The distance from westward end point of the section is given on the *horizontal axis*

The approximations $R_L^2(t)$ tend to be larger than $R^2(t)$ for small values of t and towards the end of the simulations, and $R_L^2(t)$ is smaller than $R^2(t)$ at intermediate times. In average, this model captures the mean growth of $R^2(t)$ over the tidal period well. The approximations $R_p^2(t)$ systematically overestimates the initial growth of $R^2(t)$ and underestimates this growth towards the end of the period. This is most evident for $\delta = 100$ m. Accordingly, the $R_p^2(t)$ model tends to underestimate the growth of $R^2(t)$ over the tidal period and especially for the smaller values of δ the c_1 values given in Table 3 does not reflect the true increase of $R^2(t)$.

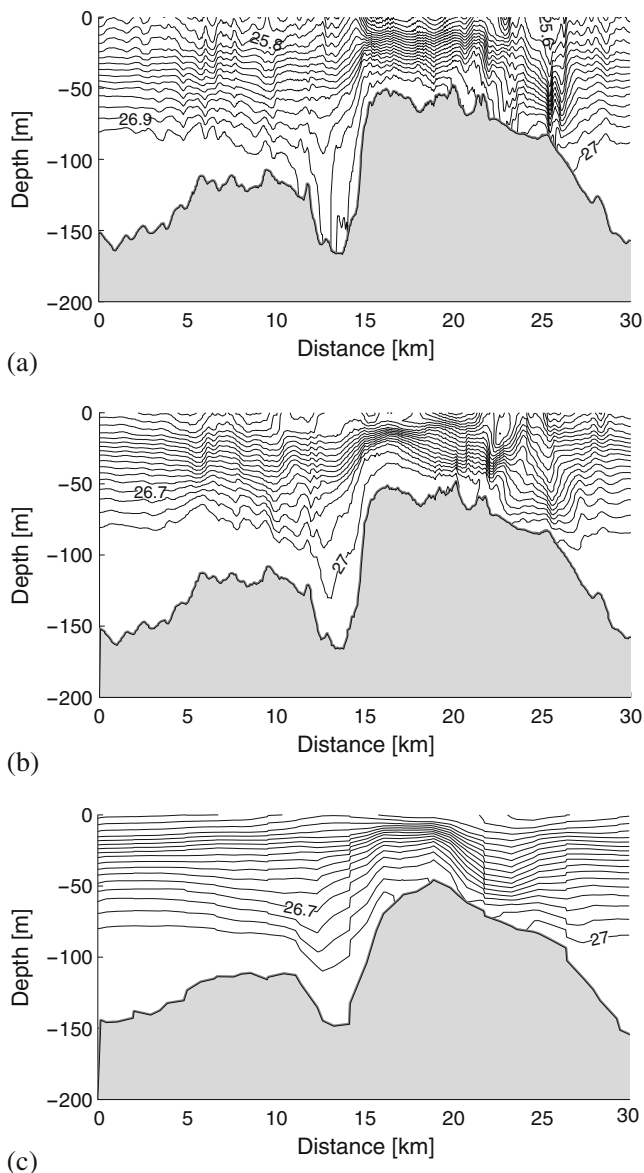


Fig. 14 Density field σ_t (kilograms per cubic metre) from the section RHOSEC in Fig. 2 at maximum inflow for **a** $\Delta x = 50$ m, **b** $\Delta x = 100$ m and **c** $\Delta x = 800$ m

The sensitivity of the mean relative dispersion $R^2(t)$ to the effects of stratification is generally smaller than the sensitivity of $R^2(t)$ to the grid size, for the range of grid sizes applied here, see Figs. 9 and 12. For the larger values of Δx , stratification tend to act against dispersion, whereas for smaller values of the grid size, the $R^2(t)$ values and the Lyapunov exponents tend to be somewhat larger under stratified conditions, see Table 2 and Fig. 12. We should bear in mind that, with the coarsest grid sizes used here, the effects of stratification are not properly represented. With $\Delta x = 50$ or 100 m, many, but far from all, features of stratified flow over topography are represented, and these processes may give an increase in the mean relative dispersion, see the discussion below and in the final section.

The density fields along a cross section (RHOSEC in Fig. 2) at maximum outflow and inflow are given in Figs. 13 and 14, respectively, for $\Delta x = 50, 100$ and 800 m. It is clearly seen that the perturbations of the iso-surfaces of density from their equilibrium levels are strongly affected by the grid size. In particular, on outflow over the steep slope outside Moskstraumen, there are indications of a hydraulic jump in the lee of the sill for $\Delta x = 100$ m. This jump becomes significantly stronger in the results produced with $\Delta x = 50$ m, see Fig. 13a. To resolve the detailed processes around hydraulic jumps an even smaller grid size and a non-hydrostatic model may be required, see Xing and Davies (2007).

4 Discussion

The study shows that, in order to accurately predict particle dispersion in Moskstraumen, we need to resolve the small-scale eddies and complexity of the current field with a grid resolution of at least 50–100 m. This will have important consequences for the development of models for coastal management, oil spill prediction and transport of pollutants, fish eggs and larvae. The vertical mixing of wind wave origin (Davies et al. 2000) also require use of high-resolution models and can be of importance for transports in the surface layer.

We have found that mean relative dispersion $R^2(t)$ is highly dependent of grid resolution Δx and also of the initial displacement δ of the particle pairs. The finer grid resolutions give the largest mean relative dispersions $R^2(T)$ after one M_2 cycle and hence also the largest growth of $R^2(t)$ shown by the Lyapunov exponent λ and the power law exponent c_1 . The Lyapunov exponent λ also increases as $\delta \rightarrow 0$, i.e. the growth of dispersion is the largest for closest initial displacement

of the particles; this is also shown in Poje et al. (2010). There is a convergence of λ and c_1 for the different grid resolutions for the particle pairs with large initial displacement δ . For large δ , we are in a regime where the separation of particles mainly are influenced by the larger eddies and dispersion is less dependent on grid resolution. For initially close particles, the subsequent separation is influenced by small-scale eddies and horizontal shears which must be resolved in order to predict the dispersion accurately. With a grid resolution of 50–100 m, our calculations indicate that we have obtained reasonably consistent values for the relative dispersion.

On a short time scale, i.e. one M_2 cycle, it was found that the mean relative dispersion $R^2(t)$ has a nearly exponential growth with an e-folding time ranging from about 2 h (50 m grid) to 10 h (800 m grid). Orre et al. (2006) also found exponential growth in their investigations in Trondheimsleia, Norway, but slower, and with an e-folding time of about one tidal cycle. The reason for the discrepancy in growth factor may be that tidal current in Trondheimsleia is less energetic than Moskstraumen and that the model used by Orre et al. (2006) did not fully resolve small-scale eddies. The exponential growth phase of $R^2(t)$ persists for the first two cycles in their experiments, thereafter closer to a power-law dependence. Poje et al. (2010) also shows an exponential growth of $R^2(t)$ on a short time scale followed by a slower growth. Separation on short time and small space scale were found to be most sensitive to the details of the advective flow and thus most dependent on the spatial resolution of the model. On long time and large space scale, their experiments showed that $R^2(t)$ was insensitive to the resolution of small-scale motions. Our results from the short time scale of one M_2 cycle are consistent with Poje et al. (2010). This emphasizes the need of high-resolution models for calculations of dispersion on short time scale and in current fields where small-scale flow features are important.

For the range of grid sizes applied here, the effect of stratification on horizontal mean relative dispersion is found to be relatively small in Moskstraumen compared to sensitivity to grid resolution. Values of λ and c_1 show only small differences between simulations with stratification and with homogeneous conditions. Our simulations with stratification give somewhat increased dispersion compared to homogeneous conditions for the finer grid resolutions. The increased dispersion may be explained by increased vertical mixing due to stratification, resolved for the finer grid resolutions. With higher spatial resolution, small-scale features of the flow such as internal waves and flow separation, see for instance Xing and Davies (2006a), may be represented. These processes may lead to a stronger

vertical velocity shear, and the horizontal dispersion may accordingly increase.

There is a considerable literature on topographic effects on stratified flow, see Thorpe (2005) and Vlasenko et al. (2005). In particular, the processes at Knight Inlet, British Columbia, Canada, have been investigated using both measurements and numerical models, see Farmer and Freeland (1983), Farmer and Armi (1999, 2001), Afanasyev and Peltier (2001a, b), Cummins et al. (2003), Klymak and Gregg (2001, 2003, 2004) and Lamb (2004). More recently, Loch Etive, Scotland, UK, has become a popular laboratory for studies of flow through shallow tidal inlets, see Inall et al. (2004, 2005), Xing and Davies (2006a, b, 2007), Davies and Xing (2007), Stashchuk et al. (2007) and Berntsen et al. (2008, 2009). The hydraulic jump found in the present results for Moskstraumen is consistent with observations and model results for Knight Inlet and Loch Etive.

Many of the numerical studies for inlets and sills have so far been performed with two-dimensional cross-section models to facilitate a high horizontal resolution. At the interface between the descending flow over sills and the stagnant body of fluid above, see Fig. 13a, small-scale overturning structures, similar to those observed at Knight Inlet (Farmer and Armi 1999), are found. Such instabilities may be modelled with cross-sectional models and a resolution close to 1 m, see Cummins et al. (2003) and Berntsen et al. (2009). With the present model area and a three-dimensional model, we are able to get into the regime in horizontal resolution where internal motion and hydraulic jumps may be represented. However, we should bear in mind that there are still unresolved processes that may be important for the small-scale mixing and also for the dispersion of particles. These unresolved processes include overturning rolls such as those observed in Knight Inlet (Farmer and Armi 1999) and also small-scale horizontal eddies ubiquitous to strong tidal inlets. In future studies with smaller grid sizes, it may also be necessary to include non-hydrostatic pressure effects, see Xing and Davies (2007) and Berntsen et al. (2009).

The staircase representation of the coastline at a headland is known to influence the eddy formation (Aldridge and Davies 1993; Davies and Jones 1996), and a boundary type coordinate unstructured mesh may be required (Signell and Geyer 1991; Jones and Davies 2008). It would be of interest to examine this effect more closely in high-resolution current models for the headland of Moskstraumen.

By using Eq. 17, we estimate the mean relative diffusivity to be of the order 10^2 – 10^3 m^2s^{-1} in

Moskstraumen. The diffusivity related to the dispersion of a cloud of particles relative to its centre of mass is proportional to relative diffusivity with a constant factor $\frac{1}{2}$ (LaCasce 2008). We have found that the relative dispersion varies strongly in Moskstraumen (as displayed in Fig. 8a, b) and accordingly also the diffusivity. Spatial variations of the dispersion coefficient has earlier been discussed by, e.g. Geyer and Signell (1992). They conclude that attempts to quantify tide-induced dispersion by a dispersion coefficient are likely to fail because such parameterization will predict uniform spreading in an area of very complex and patchy distribution. Hence, models for prediction of transport and dispersion of oil spill, fish eggs/larvae, sea lice etc., using a single diffusion coefficient, will be of limited value, unless the models actually resolves the small-scale eddies of the tidal current.

Acknowledgements This work was partly supported by the Research Council of Norway. The Norwegian Hydrographic Service, Stavanger, has provided us with a high-resolution depth matrix.

References

- Aadlandsvik B (1994) Modelling the transport of cod larvae from the Lofoten area. *ICES Mar Sci Symp* 198:379–392
- Afanasyev YD, Peltier WR (2001a) On breaking internal waves over the sill in knight inlet. *Proc R Soc Lond* 457:2799–2825
- Afanasyev YD, Peltier WR (2001b) Reply to comment on the paper on breaking internal waves over the sill in knight inlet. *Proc R Soc Lond* 457:2831–2834
- Aldridge JN, Davies AM (1993) A high-resolution three-dimensional hydrodynamic tidal model of the Eastern Irish Sea. *ICES Mar Sci Symp* 23(2):207–224
- Amundrud TL, Murray AG (2009) Modelling sea lice dispersion under varying environmental forcing in a Scottish sea loch. *J Fish Dis* 32(1):27–44
- Berntsen J (2000) Users guide for a modesplit σ -coordinate numerical ocean model. Technical report, Technical Report 135, Dept of Applied Mathematics, University of Bergen, Johs. Bruns gt.12, N-5008. Bergen, Norway, p 48
- Berntsen J, Xing JX, Davies AM (2008) Numerical studies of internal waves at a sill: sensitivity to horizontal grid size and subgrid scale closure. *Cont Shelf Res* 28(10–11):1376–1393
- Berntsen J, Xing JX, Davies AM (2009) Numerical studies of flow over a sill: sensitivity of the non-hydrostatic effects to the grid size. *Ocean Dyn* 59(6):1043–1059
- Berntsen H, Kowalik Z, Sælid S, Sørli K (1981) Efficient numerical-simulation of ocean hydrodynamics by a splitting procedure. *Model Identif Control* 2(4):181–199
- Blumberg AF, Mellor GL (1987) A description of a three-dimensional coastal ocean circulation model. In: Heaps NS (ed) *Coastal and estuarine sciences*, vol 4. Three-dimensional coastal ocean models. Xi+208p. American Geophysical Union, Washington, D.C. Illus, pp 1–16
- Burchard H, Rennau H (2008) Comparative quantification of physically and numerically induced mixing in ocean models. *Ocean Model* 20(3):293–311
- Cummins PF, Vagle S, Armi L, Farmer D (2003) Stratified flow over topography: upstream influence and generation of nonlinear waves. *Proc R Soc Lond* 459:1467–1487
- Davies AM, Jones JE (1996) Sensitivity of tidal bed stress distributions, near-bed currents, overtides, and tidal residuals to frictional effects in the Eastern Irish Sea. *J Phys Oceanogr* 26(12):2553–2575
- Davies AM, Xing J (2007) On the influence of stratification and tidal forcing upon mixing in sill regions. *Ocean Dyn* 57:431–451
- Davies AM, Kwong SCM, Flather RA (2000) On determining the role of wind wave turbulence and grid resolution upon computed storm driven currents. *Cont Shelf Re* 20(14):1825–1888
- Engedahl H, Aadlandsvik B, Martinsen EA (1998) Production of monthly mean climatological archives for the Nordic Seas. *J Mar Syst* 14(1–2):1–26
- Farmer DM, Freeland HJ (1983) The physical oceanography of fjords. *Prog Oceanogr* 12:147–220
- Farmer DM, Armi L (1999) Stratified flow over topography: the role of small-scale entrainment and mixing in flow establishment. *Proc R Soc Lond* 455:3221–3258
- Farmer DM, Armi L (2001) Stratified flow over topography: models versus observations. *Proc R Soc Lond* 457:2827–2830
- Geyer WR, Signell RP (1992) A reassessment of the role of tidal dispersion in estuaries and bays. *Estuaries* 15(2):97–108
- Gillibrand PA, Willis KJ (2007) Dispersal of sea louse larvae from salmon farms: modelling the influence of environmental conditions and larval behaviour. *Aquat Biol* 1(1): 63–75
- Gjevik B (1996) Models of drift and dispersion in tidal flows. In: Grue J et al (eds) *Waves and nonlinear processes in hydrodynamics*, 34. Kluwer Academic, Dordrecht, pp 343–354
- Gjevik B, Moe H, Ommundsen A (1997) Sources of the maelstrom. *Nature* 388(6645):837–838
- Haidvogel D, Beckmann A (1999) Numerical ocean circulation modeling. Series on environmental science and management, vol 2. Imperial College Press, London, p 318
- Haney RL (1991) On the pressure-gradient force over steep topography in sigma coordinate ocean models. *J Phys Oceanogr* 21(4):610–619
- Haza AC, Griffa A, Martin P, Molcard A, Ozgokmen TM, Poje AC, Barbanti R, Book JW, Poulain PM, Rixen M, Zanasca P (2007) Model-based directed drifter launches in the Adriatic Sea: results from the dart experiment. *Geophys Res Lett* 34(10)
- Inall M, Cottier F, Griffiths C, Rippeth T (2004) Sill dynamics and energy transformation in a jet fjord. *Ocean Dyn* 54:307–314
- Inall M, Rippeth T, Griffiths C, Wiles P (2005) Evolution and distribution of TKE production and dissipation within stratified flow over topography. *Geophys Res Lett* 32:L08607. doi:10.1029/2004GL022289
- Jones JE, Davies AM (2008) On the modification of tides in shallow water regions by wind effects. *J Geophys Res Ocean* 113(C5):C05014. doi:10.1029/2007JC004310
- Klymak JM, Gregg MC (2001) Three-dimensional nature of flow near a sill. *J Geophys Res* 106:22295–22311
- Klymak JM, Gregg MC (2003) The role of upstream waves and a downstream density pool in the growth of lee

- waves: stratified flow over the knight inlet sill. *J Phys Oceanogr* 33:1446–1461
- Klymak JM, Gregg MC (2004) Tidally generated turbulence over the knight inlet sill. *J Phys Oceanogr* 34:1135–1151
- Kowalik Z, Murty TS (1993) Numerical modeling of ocean dynamics. Advanced series on ocean engineering, vol 5. World Scientific, Singapore
- LaCasce JH (2008) Statistics from Lagrangian observations. *Prog Oceanogr* 77(1):1–29
- Lamb KG (2004) On boundary-layer separation and internal wave generation at the knight inlet sill. *Proc R Soc Lond* 460:2305–2337
- Martinsen EA, Engedahl H (1987) Implementation and testing of a lateral boundary scheme as an open boundary-condition in a barotropic ocean model. *Coast Eng* 11(5–6):603–627
- Mellor G (1996) User guide for three-dimensional, primitive equation, numerical ocean model. Technical report, Technical report, Princeton University.
- Mellor GL, Yamada T (1982) Development of a turbulence closure-model for geophysical fluid problems. *Rev Geophys* 20:851–875
- Mellor GL, Oey LY, Ezer T (1998) Sigma coordinate pressure gradient errors and the seamount problem. *J Atmos Ocean Technol* 15(5):1122–1131
- Mitchelson-Jacob G, Sundby S (2001) Eddies of Vestfjorden, Norway. *Cont Shelf Res* 21(16–17):1901–1918
- Moe H, Ommundsen A, Gjevik B (2002) A high resolution tidal model for the area around the Lofoten Islands, northern Norway. *Cont Shelf Res* 22(3):485–504
- Ommundsen A (2002) Models of cross shelf transport introduced by the Lofoten Maelstrom. *Cont Shelf Res* 22(1):93–113
- Orre S, Gjevik B, Lacasce JH (2006) Characterizing chaotic dispersion in a coastal tidal model. *Cont Shelf Res* 26(12–13):1360–1374
- Poje AC, Haza AC, Özgökmen TM, Magaldi MG, and Garraffo ZD (2010) Resolution dependent relative dispersion statistics in a hierarchy of ocean models. *Ocean Model* 31(1–2):36–50
- Proctor R, Elliot AJ, Flather RA (1994) Forecast and hindcast simulations of the Braer oil-spill. *Mar Pollut Bull* 28(4):219–229
- Reed M, Ekrol N, Rye H, Turner L (1999a) Oil spill contingency and response (Oscar) analysis in support of environmental impact assessment offshore Namibia. *Spill Sci Technol Bull* 5(1):29–38
- Reed M, Johansen O, Brandvik PJ, Daling P, Lewis A, Fiocco R, Mackay D, Prentki R (1999b) Oil spill modeling towards the close of the 20th century: overview of the state of the art. *Spill Sci Technol Bull* 5(1):3–16
- Rennau H, Burchard H (2009) Quantitative analysis of numerically induced mixing in a coastal model application. *Ocean Dyn* 59(5):671–687
- Ridderinkhof H, Zimmerman JTF (1992) Chaotic stirring in a tidal system. *Science* 258(5085):1107–1111
- Signell RP, Geyer WR (1991) Transient eddy formation around headlands. *J Geophys Oceans* 96(C2):2561–2575
- Signell RP, Butman B (1992) Modeling tidal exchange and dispersion in Boston Harbor. *J Geophys Oceans* 97(C10):15591–15606
- Skarðhamar J, Slagstad D, Edvardsen A (2007) Plankton distributions related to hydrography and circulation dynamics on a narrow continental shelf off northern Norway. *Estuar Coast Shelf Sci* 75(3):381–392
- Slagstad D, Tande KS, (2007) Structure and resilience of overwintering habitats of *Calanus finmarchicus* in the Eastern Norwegian Sea. *Deep-Sea Res Part II Top Stud Oceanogr* 54(23–26):2702–2715
- Smagorinsky J (1963) General circulation experiments with the primitive equations. *Mon Weather Rev* 91(3):99–164
- Stashchuk N, Inall M, Vlasenko V (2007) Analysis of supercritical stratified tidal flow in a Scottish fjord. *J Phys Oceanogr* 37:1793–1810
- Thorpe SA (2005) The turbulent ocean. Cambridge University Press, Cambridge
- Vikebø F, Jørgensen C, Kristiansen T, Fiksen O (2007) Drift, growth, and survival of larval Northeast Arctic cod with simple rules of behaviour. *Mar Ecol Prog Ser* 347:207–219
- Vlasenko VI, Stashchuk N, Hutter K (2005) Baroclinic tides: theoretical modeling and observational evidence. Cambridge monographs on mechanics. Cambridge University Press, Cambridge
- Wahl T (1995) The Maelström seen from space. *Nord Space Act* 2–3:22–23
- Xing J, Davies A (2006a) Processes influencing tidal mixing in the region of sills. *Geophys Res Lett* 33(4):L04603. doi:[10.1029/2005GL025226](https://doi.org/10.1029/2005GL025226)
- Xing JX, Davies AM (2006b) Influence of stratification and topography upon internal wave spectra in the region of sills. *Geophys Res Lett* 33(23):L23606. doi:[10.1029/2006GL028092](https://doi.org/10.1029/2006GL028092)
- Xing JX, Davies AM, (2007) On the importance of non-hydrostatic processes in determining tidally induced mixing in sill regions. *Cont Shelf Res* 27:2162–2185
- Yang HQ, Przekwas AJ (1992) A comparative-study of advanced shock-capturing schemes applied to Burgers-equation. *J Comput Phys* 102(1):139–159
- Zimmerman JTF (1986) The tidal whirlpool—a review of horizontal dispersion by tidal and residual currents. *Neth J Sea Res* 20(2–3):133–154